Atomically Dispersed Single Ni Site Catalysts for Nitrogen Reduction toward Electrochemical Ammonia Synthesis Using N_2 and H_2O

Shreya Mukherjee, Xiaoxuan Yang, Weitao Shan, Widitha Samarakoon, Stavros Karakalos, David A. Cullen, Karren More, Maoyu Wang, Zhenxing Feng,* Guofeng Wang,* and Gang Wu*

Ammonia (NH_3) electrosynthesis gains significant attention as NH_3 is essentially important for fertilizer production and fuel utilization. However, electrochemical nitrogen reduction reaction (NRR) remains a great challenge because of low activity and poor selectivity. Herein, a new class of atomically dispersed Ni site electrocatalyst is reported, which exhibits the optimal NH_3 yield of 115 µg cm^{-2} h^{-1} at –0.8 V versus reversible hydrogen electrode (RHE) under neutral conditions. High faradic efficiency of 21 ± 1.9% is achieved at –0.2 V versus RHE under alkaline conditions, although the ammonia yield is lower. The Ni sites are stabilized with nitrogen, which is verified by advanced X-ray absorption spectroscopy and electron microscopy. Density functional theory calculations provide insightful understanding on the possible structure of active sites, relevant reaction pathways, and confirm that the Ni-N_3 sites are responsible for the experimentally observed activity and selectivity. Extensive controls strongly suggest that the atomically dispersed NiN_3 site-rich catalyst provides more intrinsically active sites than those in N-doped carbon, instead of possible environmental contamination. This work further indicates that single-metal site catalysts with optimal nitrogen coordination is very promising for NRR and indeed improves the scaling relationship of transition metals.

1. Introduction

Due to its high energy density (4.32 kWh L^{-1}), hydrogen content (17.6 wt%), and facile liquidation (boiling point: –33.3 °C at 1 atm), ammonia (NH_3) is used as a clean alternative fuel and hydrogen carrier for storage and delivery. Currently, ammonia synthesis is a significant chemical technology and heavily dependent upon the traditional Haber–Bosch process with the harsh condition from gaseous nitrogen and hydrogen, which consumes 1–2% of the world's annual energy supply consumption and is not environmentally friendly. In view of the fossil fuels shortage and global climate change, a clean and sustainable route for efficient N_2 fixation is desired.[1] Electrochemical nitrogen reduction reaction (NRR) is emerging as a very attractive strategy for sustainable development, as it utilizes renewable electricity to convert water and N_2 into NH_3 under ambient conditions.[2] Especially, the utilization of H_2O as the hydrogen source instead of raw material hydrogen can substantially reduce energy intensive process of hydrogen production from methane or natural gas, as well as fossil fuels and greenhouse gas emission.[3] However, to date, NH_3 production efficiency via NRR remains unsatisfactory. The greatest challenge is the impractically low Faradaic efficiency (FE) due to the competing hydrogen evolution reaction (HER) that occurs in the same region of potential.[4] Previously, a variety of metal and metal-free active sites have been explored as possible electrocatalysts for the NRR,[5–10] which are summarized in Table S1 and S2, Supporting Information, respectively. Unfortunately, in most of these studies, the catalytic performances were still insufficient to be practical for the production of NH_3.

S. Mukherjee, X. Yang, Prof. G. Wu
Department of Chemical and Biological Engineering
University at Buffalo
The State University of New York
Buffalo, NY 14260, USA
E-mail: gangwu@buffalo.edu

W. Shan, Prof. G. F. Wang
Department of Mechanical Engineering and Materials Science
University of Pittsburgh
Pittsburgh, PA 15261, USA
E-mail: guw8@pitt.edu

The ORCID identification number(s) for the author(s) of this article can be found under https://doi.org/10.1002/smtd.201900821.

W. Samarakoon, M. Wang, Prof. Z. Feng
School of Chemical, Biological, and Environmental Engineering
Oregon State University
Corvallis, OR 97331, USA
E-mail: zhenxing.feng@oregonstate.edu

Dr. S. Karakalos
Department of Chemical Engineering
University of South Carolina
Columbia, SC 29208, USA

Dr. D. A. Cullen, Prof. K. More
Materials Science and Technology Division
Oak Ridge National Laboratory
Oak Ridge, TN 37831, USA

Recently, single-metal site catalysts have provided new opportunities toward NRR and enable effective suppression of the HER.[11–15] For example, Choi et al. indicated that NRR selectivity on single metal sites is significantly higher than that on bulk metals surfaces due to the effective suppression of the HER with the help of ensemble effect.[16] Nørskov and co-workers found that "on top" binding of nitrogen that is possible on single metal sites can enhance the rate of NH_3 synthesis.[17] Moreover, it has been found that N species can promote the dissociation of N_2, especially in the presence of single-metal Lewis acid ions.[15] However, stabilizing the isolated single atoms against migration and agglomeration due to the high surface energy is one of the key challenges during the synthesis. Compared to synthetic methods such as atomic layer deposition, atomic layer trapping, etc., utilization of metal organic frameworks (MOFs) to fabricate atomically dispersed catalysts has recently attracted considerable attention.[18,19] One of the strategies to form atomically dispersed species is to utilize the unique pores of MOFs as cages to spatially confine metallic species.[20] The other effective strategy is to construct defect-rich carbon hosts via a pyrolysis of MOFs as hosts, which can trap metal precursors and stabilize isolated metal atoms during the following thermal activation via an enhanced charge transfer mechanism between single atoms and defective sites.[19,21]

Here, we report atomically dispersed Ni sites on carbon framework with nitrogen vacancy as an effective non-noble metal electrocatalyst for the NRR through a defect engineering strategy and pyrolysis of bimetallic metal organic framework (BMOF) of Ni and Zn. As a control, we also synthesized Ni clusters supported on N-doped carbon framework and no significant NRR activity was observed, confirming atomically dispersed unsaturated Ni coordination was the true active sites that was identified and investigated by X-ray absorption spectroscopy (XAS) and advanced scanning transmission electron microscopy (STEM) coupled with electron energy loss spectra (EELS) at the atomic level. The single Ni site catalyst showed the highest NH_3 production rate of 115 µg cm^{-2} h^{-1} at –0.8 V versus reversible hydrogen electrode (RHE) and maximum FE of 20% at –0.6 V versus RHE under neutral condition. Under alkaline condition, highest FE of 21 ± 1.9% was attained at –0.2 V vs RHE, although the yield of ammonia was found to be lower than under neutral condition. Furthermore, density functional theory (DFT) calculations provide insightful understanding on the possible structure of active sites and favorable reaction pathway of the NRR on the single Ni site catalyst. The resulting catalyst may expand to other single metal sites such as Mo, Sc, V, and Zr for developing non-noble metal single site catalysts, which likely yield enhanced NRR activity and selectivity for ammonia synthesis.

2. Results and Discussion

2.1. Morphology and Coordination of Unsaturated Ni

An effective method was developed to form Ni-N$_x$-C coordination from controlled pyrolysis of a BMOF of Ni and Zn (Ni$_x$Zn$_{(1-x)}$BMOF). This process is also known as chemical doping of Ni into ZIF-8.[22] During the formation of the BMOF, Ni substitutes some of Zn nodes during crystallization (**Figure 1**a). Thus, it coordinates with the ligands similarly as Zn without affecting the structure. The morphology of Ni$_x$Zn$_{(1-x)}$BMOF is similar to that of ZIF-8, showing sodalite-type crystal structure and the rhombic dodecahedron shape (Figure S1a,b, Supporting Information). X-ray diffraction (XRD) patterns of Ni$_x$Zn$_{(1-x)}$BMOF and Ni-N$_x$-C before (Figure 1b) and after pyrolysis (Figure 1c) indicate similar phases to ZIF-8 and amorphous carbon, respectively. High-resolution transmission electron microscopy (HRTEM) images of the Ni-N$_x$-C catalyst show a typical porous carbon framework without any metallic nanoparticles (Figure 1d,e). Besides, the brighter spots were observed in the high-angle annular dark-field STEM mode compared to C and N atoms, further confirming that Ni atoms are homogeneously distributed in the carbon support (Figure 1f,g). EELS at the bright spots shows the coexistence of Ni and N signals (Figure 1h,i) while the spectra on the carbon does not show any peak for Ni (Figure 1j,k).

Extended X-ray absorption fine structure (EXAFS) and X-Ray absorption near edge structure (XANES)[23] were performed to investigate the state of Ni species and their coordination environments (Figure 1l–n). Figure 1l indicates that Ni-N$_x$-C has a higher oxidation state than Ni foil but a lower oxidation state than NiO. Small peaks at 8334 and 8338 eV are very close to the peaks of NiN$_4$ coordination of Ni phthalocyanines.[24] The pre-edge peak near 8334 eV is assigned to the dipole forbidden but quadrupole-allowed transition (1s→3d), which indicates 3d and 4p orbital hybridization of the Ni central atoms.[24] The peak at 8338 eV indicates 1s→ 4p transition and is consistent with a pyramidal geometry for Ni single sites.[25] In addition, no peak corresponding to Ni-C coordination is observed at 8343 eV.[26] The K^2-weighted Fourier transform of Ni K-edge EXAFS oscillation shows a distinct peak at 1.41 Å (Figure 1m), which arises from the first shell Ni-N coordination.[27] As expected, no dominant peak corresponding to Ni-C coordination is observed at 1.2 or 1.6 Å. However, a small broad peak at 0.8 Å is observed for superposition of peaks due to Ni-N and Ni-C coordination.[28] The coordination number of Ni-N is 3.4 (Table S3, Supporting Information). Considering the error of EXAFS fitting, it can be inferred that the true Ni-N coordination is between 3 and 4 and the Ni atoms are coordinatively unsaturated. Figure 1n shows the EXAFS fits of NiPc and Ni-N$_x$-C in k-space and the oxidation state of Ni is between 0 and +2 as suggested from XANES. Zn K-edge XAS is also performed (Figure S2c,d, Supporting Information) since Zn is still in the original structure at the pyrolysis temperature. The EXAFS results indicate that Zn is coordinated with nitrogen in Zn-N$_4$ coordination at 700 °C for 3 h (Figure S3c,d and Table S3, Supporting Information). To investigate the importance of Zn-N$_4$ in NRR, we also tested ZIF-8 that was pyrolyzed at 700 °C for 3 h. Although it is active for NRR, the activity is much lesser than that of Ni-N$_x$-C (discussed later). Thus, Zn-N$_4$ probably acts as spacers to prevent Ni aggregation in Ni-N$_x$-C, instead of highly active NRR sites.

2.2. Catalyst Preparation at Various Conditions

Carbonization conditions proved effective in adjusting the level of nitrogen doping and the degree of graphitization in

ADVANCED
SCIENCE NEWS

www.advancedsciencenews.com

small
methods

www.small-methods.com
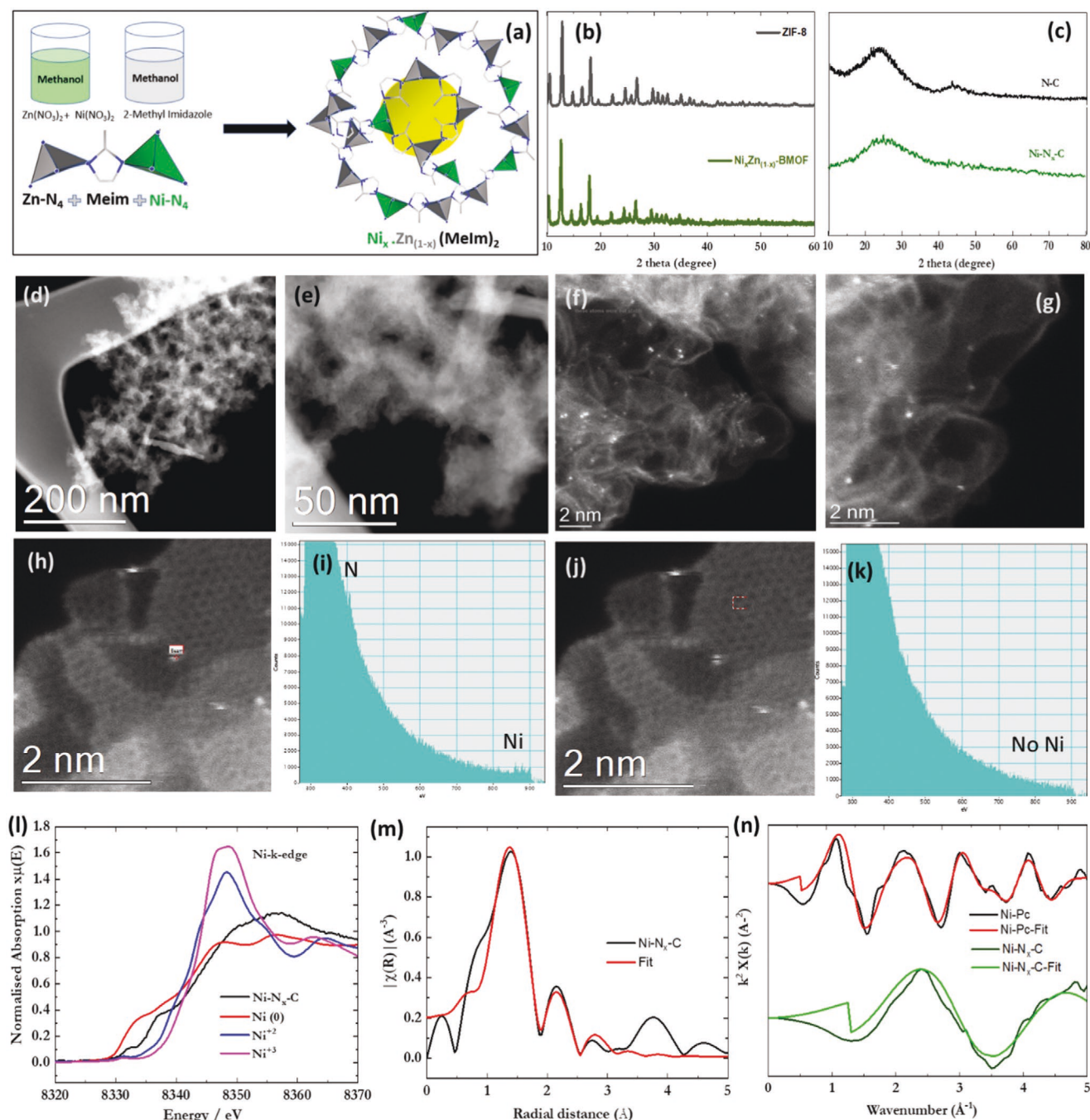
Figure 1. a) Schematic of $Ni_xZn_{(1-x)}$BMOF. b) XRD of $Ni_xZn_{(1-x)}$BMOF (represented in green) and ZIF-8 (represented in black). c) XRD of Ni-N_x-C (represented in green) and N-C (represented in black). d,e) HRTEM of Ni-N_x-C. f,g) High-angle annular dark-field STEM of Ni-N_x-C, showing distribution of bright spots. h–k) EELS of Ni-N_x-C. l) XANES of Ni-N_x-C. m) Fourier-transformed EXAFS data and of Ni-N_x-C. n) EXAFS fits of NiPc and Ni-N_x-C in k-space.

carbon structures.[29,30] The change in carbon structure with pyrolysis conditions was investigated using Raman spectroscopy (**Figure 2**a). Additionally, to get more understanding on the Ni coordination, N-doping, and their correlation with pyrolysis conditions, X-ray photoelectron spectroscopy (XPS) analysis was performed (Figure 2b,c).

From Figure 2a, two characteristic carbon resonances around 1600 cm^{-1} (G band) and 1380 cm^{-1} (D band) are dominant,

which correspond to the planar motion of sp^2-hybridized carbon atoms in an ideal plane and at the edge, respectively.[29,31,32] The ratio of the intensities of the two peaks (I_D/I_G) indicates the overall degree of graphitization in carbon. I_D/I_G ratio of Ni-N_x-C-600-3h is only 0.87 that implies the lack of defect formation and low degree of graphitization at 600 °C. In addition, another characteristic carbon resonance around 2700 cm^{-1} (referred as 2D peak) is also observed in each catalyst. The 2D
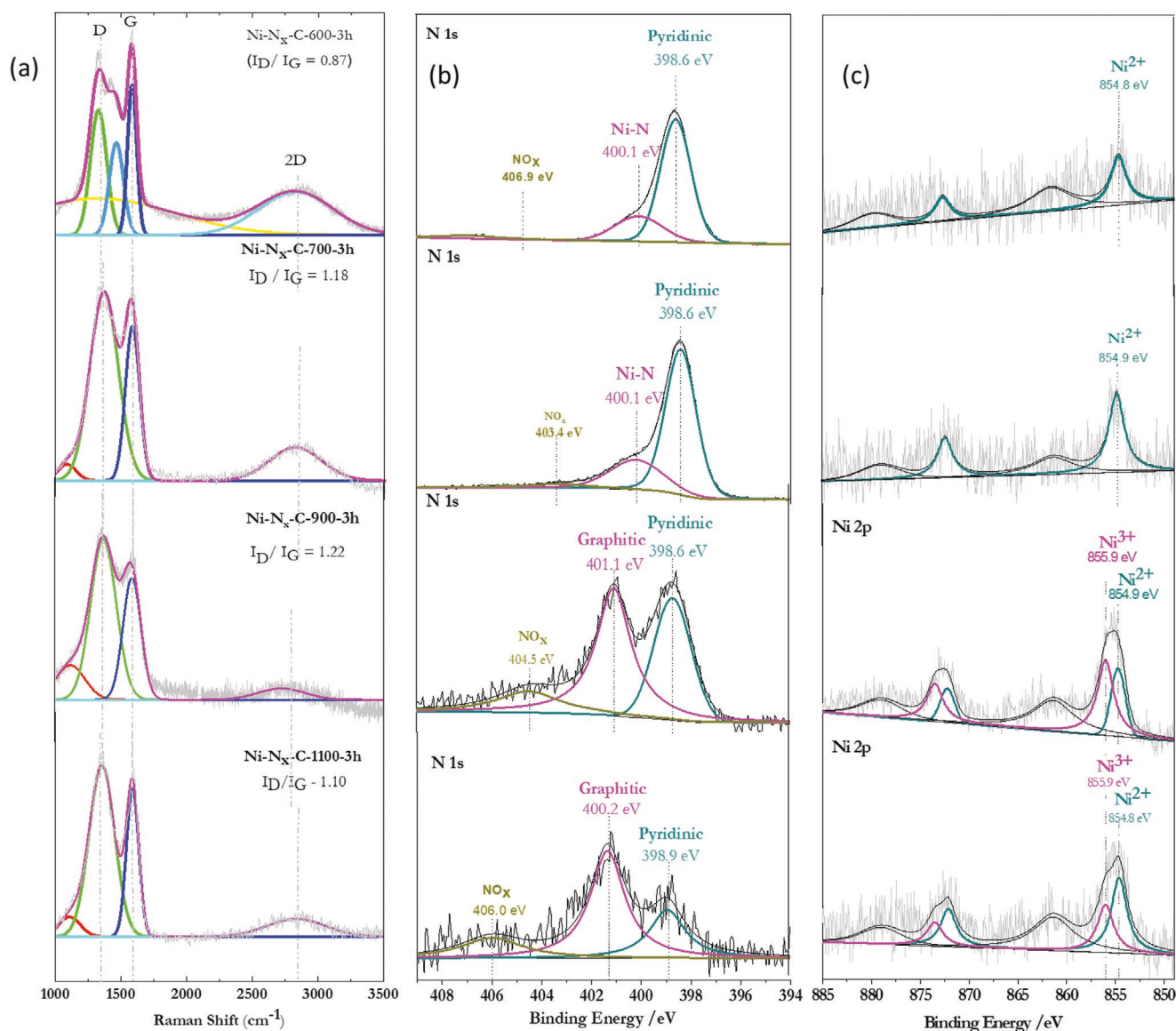
Figure 2. a) Raman spectroscopy, b) XPS N1s, and c) XPS Ni 2p of $Ni_xZn_{(1-x)}$BMOF pyrolyzed at 600, 700, 900, 1100 °C (from top to bottom, respectively).

peak is the second order of the D peak that is always present in graphene and is not correlated with any defect.[33] However, the intensity of 2D band decreases with increasing layers as well as doping concentration. The position of the 2D peak shows red shift (>2700 cm^{-1}) for Ni-N_x-C-600-3h, Ni-N_x-C-700-3h, Ni-N_x-C-900-3h, as well as Ni-N_x-C-1100-3h that is typical for N doping in graphene.[34] As the pyrolysis temperature increases, the height of 2D peak sharply decreased, probably due to increase in defect concentration and high degree of graphitization at higher pyrolysis temperature. In addition, two broad signals at ≈1200 and 1510 cm^{-1} are associated with the carbon atoms outside of a perfectly planar sp^2 carbon network (such as aliphatic or amorphous structures) and integrated five-member rings or heteroatoms in carbon layers, respectively. Comparison of I_D/I_G ratio at other pyrolysis conditions is shown in Table S4, Supporting Information. For Ni-N_x-C-700-3h, more ordered

sp^2 carbon was formed relative to Ni-N_x-C-600-3h with broad peak between D and G peaks. Less carbon defects and disordered structures are identified in catalysts treated at high temperature such as Ni-N_x-C-900-3h and Ni-N_x-C-1100-3h, which is not favorable for the formation of single Ni sites. This is in good agreement with the N1s XPS analysis, suggesting no obvious Ni-N coordination at 400.1 eV (Figure 2b). In addition, as shown in Figure 2c, the binding energy of Ni 2p XPS spectrum is ≈855 eV (854.9 eV), which is higher than that of metallic Ni (853.0 eV) and lower than that of Ni^{2+} in Ni pc (855.7 eV), indicating that Ni has a valence between 0 and +2 and is unsaturated.[35]

The elemental quantification determined by XPS is listed in Table S6, Supporting Information. Different N configuration doped in carbon after pyrolysis of MOFs can be identified by the difference in binding energy: pyridinic (398.4 ± 0.2 eV),

**ADVANCED
SCIENCE NEWS**

www.advancedsciencenews.com

**small
methods**

www.small-methods.com

metal–N (399.6 ± 0.2 eV), pyrrolic (400.8 ± 0.2 eV), graphitic nitrogen (401.1 ± 0.2 eV), and nitrogen oxides (>404.0 eV).[36] Pyridinic and graphitic nitrogen atoms are at the edge and interior of the carbon planes, respectively, while pyrrolic N is in a five-side carbon ring. When pyrolyzed at 700 °C for 3 h, pyridinic nitrogen is dominant and no graphitic nitrogen is observed. However, with increasing the pyrolysis temperature, graphitic nitrogen becomes dominant. As we reported earlier, pyridinic nitrogen content is critical for NRR activity while graphitic nitrogen is known to favor HER.[37] Therefore, NRR activity decreased with increasing the pyrolysis temperature, which may be related to the increase of graphitic nitrogen as well as the lack of Ni-N coordination.

In addition, Ni-N_x-C-700-3h catalyst has a BET surface area of 270 m^2 g^{-1} with a pore volume of 0.812 cm^3 g^{-1} (Table S7, Supporting Information). Unlike metal aggregates, nano-clusters or single nickel do not completely occupy the micropores (Figure S4, Supporting Information). XRD at all those pyrolysis conditions are compared in Figure S5, Supporting Information. Small clusters and aggregates are observed in the XRD of BMOF pyrolyzed at 700 °C for 1 h and 900 °C for 1 h; however, no such aggregates are observed for any other catalysts.

2.3. Catalyst Optimization for Electrochemical Ammonia Synthesis

The standard absorbance spectra and calibration curve for ammonia detection in 0.1 M KOH solution using sodium salicylate method is shown in Figure S6, Supporting Information. Catalytic activity at different pyrolysis conditions is shown in **Figure 3**a when tested at –0.3 V versus RHE (optimum potential). NRR activity is the highest when pyrolyzed for 3 h (Figure S7, Supporting Information); thus, the study is focused on Ni-N_x-C-700-3h. Although a small amount of ammonia was detected for the $Ni_xZn_{(1-x)}$BMOF precursor, it was similar in both N_2 and Ar atmosphere and much lesser than the sample after pyrolysis, likely due to from the nitrogen species in precursors. Importantly, NRR activity is the highest for a sample obtained from pyrolysis conditions of 700 °C for 3 h and the activity decreased with increasing temperatures of pyrolysis.

Figure 3b shows the correlation between partial current density and FE for catalysts pyrolyzed under different conditions. The current density in Ar is higher than N_2 for the $Ni_xZn_{(1-x)}$BMOF pyrolyzed at temperatures above 900 °C. This can be correlated with the presence of Ni as
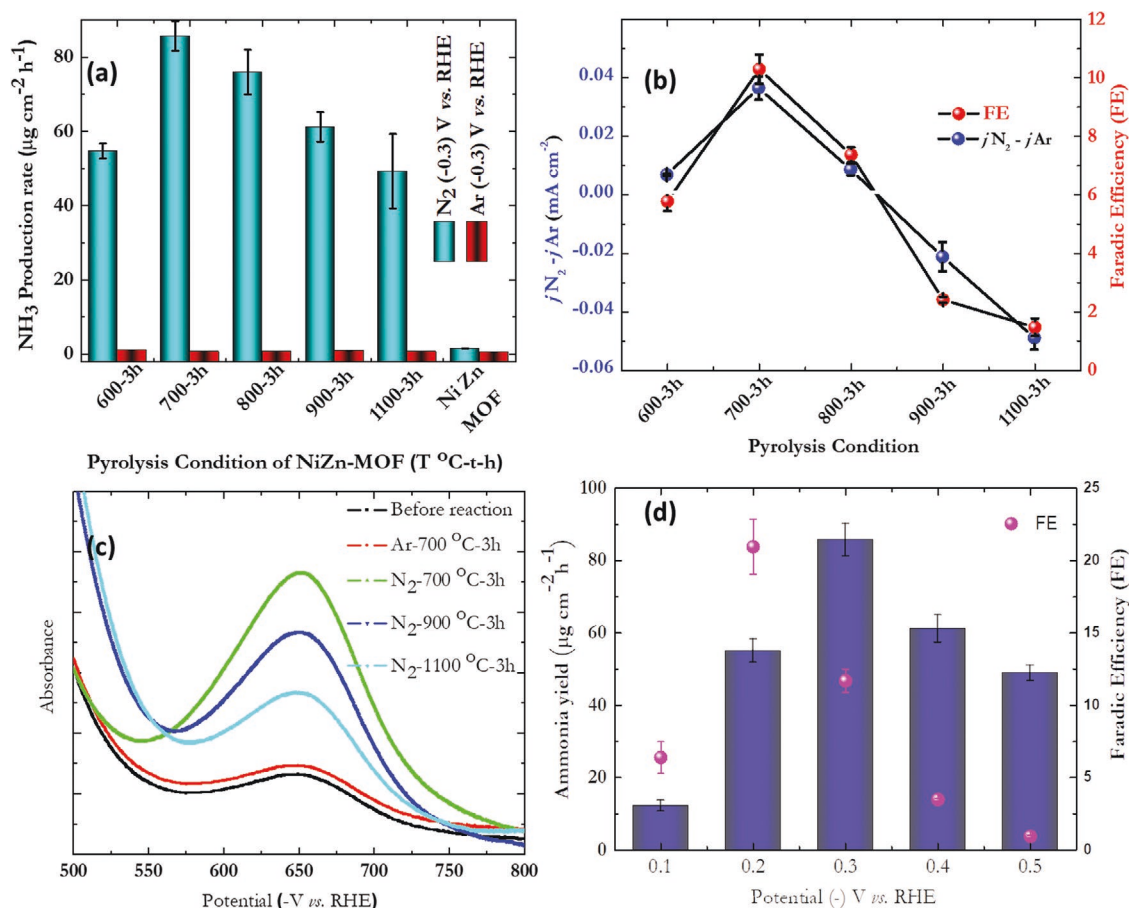
Figure 3. a) Comparison of NH_3 production rate at different pyrolysis conditions at –0.3 V versus RHE in 0.1 M KOH solution. b) Comparison of partial current density and FE as function of pyrolysis condition for $Ni_xZn_{(1-x)}$BMOF at –0.3 V versus RHE in 0.1 M KOH solution. c) Comparison of UV–vis absorbance spectra after potentiostatic tests in 0.1 M KOH solution for the NRR on $Ni_xZn_{(1-x)}$BMOF pyrolyzed at different temperatures for 3 h. d) Comparison of NH_3 production rate and FE as function of potential during the NRR for Ni-N_x-C-700-3h in 0.1 M KOH solution.

**ADVANCED
SCIENCE NEWS**
www.advancedsciencenews.com

**small
methods**
www.small-methods.com

aggregates rather than single atoms for Ni$_x$Zn$_{(1-x)}$BMOF pyrolyzed at temperatures above 900 °C that increases the extent of HER even at –0.3 V versus RHE. Figure 3c shows the corresponding UV–vis spectra and Figure 3d provided a comparison of activity at various potentials for the best performing Ni-N$_x$-C-700-3h catalyst. The ammonia production rate in 0.1 M KOH solution was 85 µg cm^{-2} h^{-1} at –0.3 V versus RHE with a FE of around 11%. However, the FE is approximately 20% at –0.2 V versus RHE but with relatively low production rates. The activity is also two times higher than the metal-free nitrogen-doped carbon catalyst that we had reported earlier at the same potential.[5] At –0.4 V versus RHE, the ammonia yield was slightly higher than that of –0.2 V versus RHE, although the FE is decreased due to dominance of HER.

To measure the background ammonia and contamination from the electrode itself, we tested the linear sweep voltammetry (LSV) of the glassy carbon electrode without catalysts in N$_2$ and Ar atmosphere, respectively. As shown in Figure S8a, Supporting Information, the current density is much lower than when Ni-N$_x$-C is used as the catalyst. In addition, chronoamperometry tests in different potential in N$_2$ and Ar were also run using glassy carbon electrode to measure ammonia under experimental conditions in Figure S8b, Supporting Information. It can be seen that very little or no NH$_3$ is detected, confirming that the original source of NH$_3$ was generated from electroreduction of N$_2$ by the studied catalysts, rather than from environments.

Durability is considered as an important criterion to evaluate catalytic performance. Figure S9d, Supporting Information, shows the difference in current density in N$_2$ and Ar atmosphere when tested for about 20 h. The LSV before and after stability test in nitrogen shows no degradation in current density (Figure S9e, Supporting Information). The ammonia production rate and FE measured after each cycle are also comparable and steady (Figure S9f, Supporting Information), indicating the excellent stability of our catalyst for NRR.

2.4. Control Experiments

To confirm whether the unsaturated Ni-N$_x$-C is the true active sites, we synthesized Ni clusters on N-doped carbon (Ni$_{clusters}$-N-C) derived from Ni-MOF-74 with Ni as the only metal and N-C derived from ZIF-8 as comparisons. Comparisons of the XRD patterns before and after pyrolysis are shown in **Figure 4**a,b, respectively. Ni clusters are distinctly observed from the Ni$_{clusters}$-N-C sample with strong peaks at 45°, 52°, and 76°, representing crystal faces of Ni (111), Ni (200), and Ni (220), respectively, (JCPDS card no #40850), as well as some peaks of NiO (100) at 32° and NiO (111) at 37° (JCPDS card no #47-1049), indicating the presence of metallic aggregates. However, no diffraction peaks for Ni, NiO, Zn, or ZnO are observed in the Ni-N$_x$-C sample, which suggested that mixing of Zn not only helps in
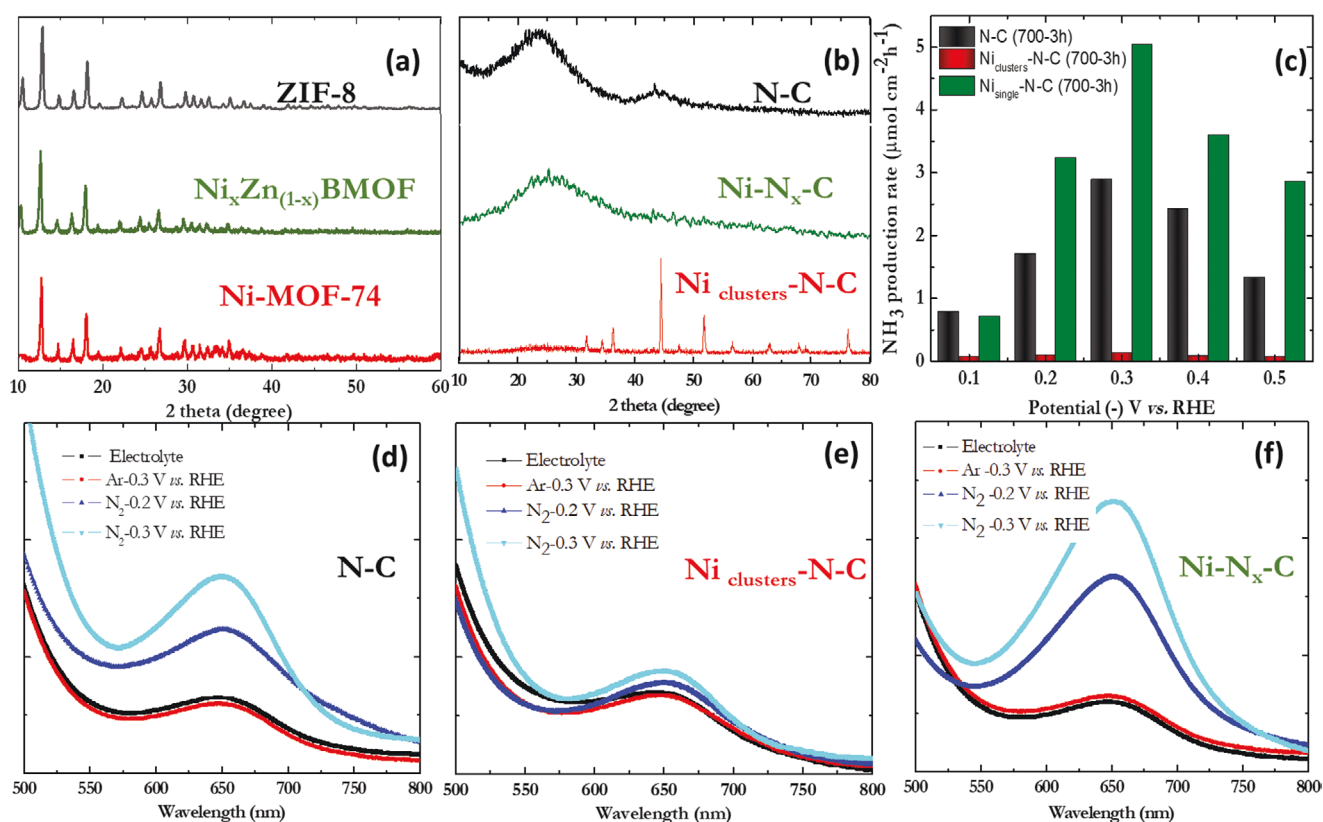
Figure 4. Comparison of XRD of a) ZIF-8 (black), Ni$_x$Zn$_{(1-x)}$BMOF (green), and Ni-MOF-74 (red). b) Pyrolyzed ZIF-8 (N-C, black), Ni-N$_x$-C-700-3h (green), and Ni$_{clusters}$-N-C (red). c) Ammonia production rate comparison for N-C, Ni$_{clusters}$-N-C, and Ni-N$_x$-C. UV–vis spectroscopy of d) N-C, e) Ni$_{clusters}$-N-C, and f) Ni-N$_x$-C tested in 0.1 M KOH solution, respectively.

ADVANCED
SCIENCE NEWS
www.advancedsciencenews.com

small
methods
www.small-methods.com

obtaining the porous structure but also acts as a spacer to prevent formation of Ni aggregates.[36]

NRR activity with variation of negative potential for N-C, $Ni_{clusters}$-N-C, and $Ni-N_x$-C are shown in Figure 4c and the corresponding UV–vis spectroscopies are shown in Figure 4d–f, respectively. For $Ni_{clusters}$-N-C, the ammonia detected is similar in N_2 and Ar atmosphere with no net NRR activity when tested in the potential range of 0 to –0.5 V versus RHE. However, a strong difference in absorbance peak between N_2 and Ar is observed for $Ni-N_x$-C, which is also higher than that of N-C synthesized under identical pyrolysis conditions.

2.5. Ammonia Synthesis in Different Electrolytes

We compared the catalytic activity of NRR using three different electrolytes: 0.1 M KOH (pH = 13), 0.5 M $LiClO_4$ (pH = ≈8), and 0.01 M HCl (pH = 1). Higher the concentration of acid, higher the HER activity; thus, we chose 0.01 M HCl as the electrolyte under acidic conditions. Similarly, extent of HER is higher for highly concentrated alkali. Thus, 0.1 M KOH was chosen as the electrolyte under alkaline conditions. Initially, we compared current densities in different Ar-saturated electrolytes to eliminate electrolytes that highly favor HER (Figure S10, Supporting Information). The current

densities of 0.1 M HCl and 0.1 M $HClO_4$ solutions in Ar are similar, indicating that they have similar HER activities, while current densities in the 0.05 M H_2SO_4 solution is higher than that in 0.05 M HCl solution. This is probably due to dibasic nature of H_2SO_4. Although the pH of the electrolytes is different, they have similar specific conductivity. For 0.1 M KOH solution, specific conductance at 25 °C is 0.0241 S cm^{-1},[38] it is 0.0367 S cm^{-1} for 0.5 M $LiClO_4$ solution,[39] and 0.0324 S cm^{-1} for 0.01 M HCl.[40]

In addition, the comparison of current density in N_2 and Ar and the standard calibration curve along with UV–vis absorbance spectra in 0.5 M $LiClO_4$ solution is shown in Figure S11, Supporting Information. The catalyst achieves the highest NH_3 yield of 115 µg cm^{-2} h^{-1} at –0.8 V versus RHE and the highest FE of 18.5 ± 3% at –0.6 V versus RHE (Figure S12, Supporting Information, **Figure 5**a,b). Furthermore, we further tried to improve NRR activity of our catalyst at a slightly higher temperature but ambient pressure in 0.5 M $LiClO_4$ solution. The activity slightly increased at 40 °C but decreased again at 60 °C (Figure S13, Supporting Information).

Figure 5c shows the UV–vis absorbance spectra of the best performing $Ni-N_x$-C-700-3h catalyst at different potentials in 0.01 M HCl solution. The corresponding current densities in N_2 and Ar at different potentials are shown in Figure S14, Supporting Information, with the standard calibration curve
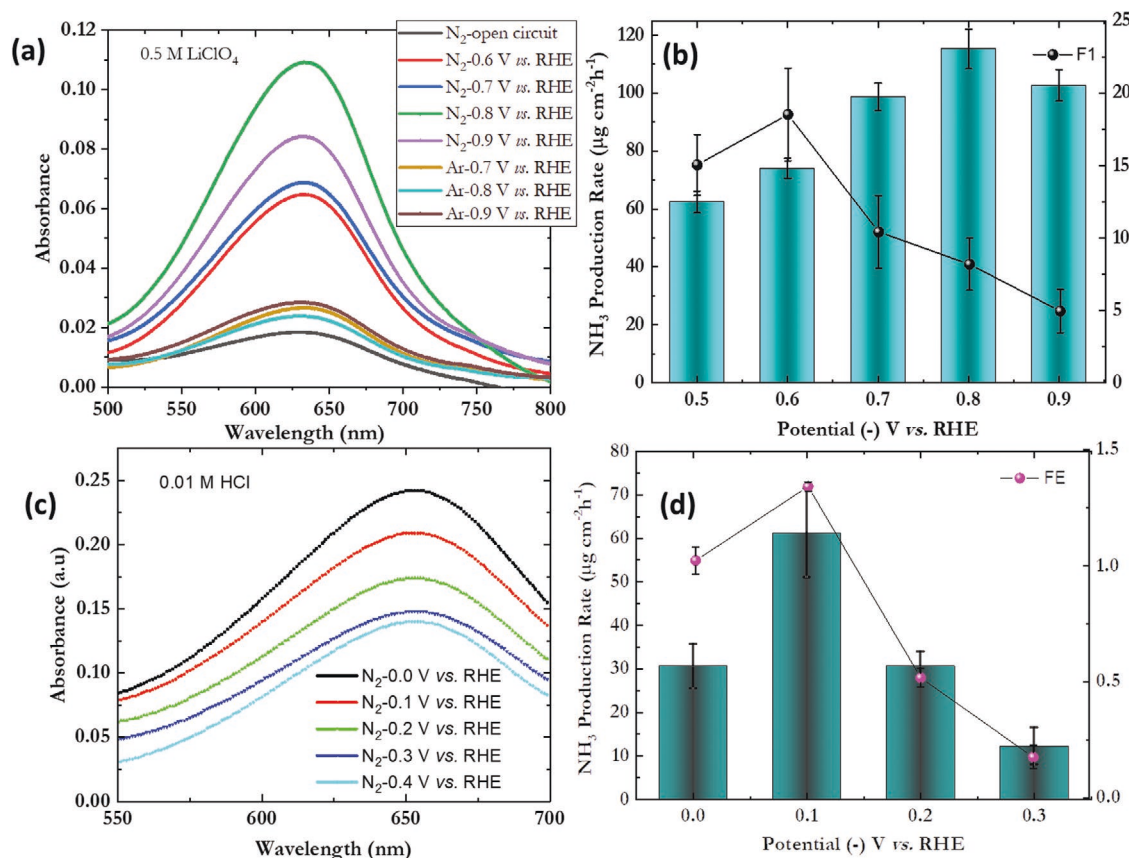
Figure 5. Comparison of a) UV–vis absorbance spectra after potentiostatic tests and b) ammonia production rates and FE for Ni_x-N-C-700-3h catalyst in 0.5 M $LiClO_4$ solution. c) Comparison of UV–vis absorbance spectra after potentiostatic tests and d) ammonia production rates and FE for Ni_x-N-C-700-3h catalyst in 0.01 M HCl solution.

**ADVANCED
SCIENCE NEWS**
www.advancedsciencenews.com

**small
methods**
www.small-methods.com

in Figure S15, Supporting Information. Using 0.01 M HCl as the electrolyte, the onset potential for NRR was found to be at 0 V versus RHE while the highest activity was obtained at –0.1 V versus RHE (Figure 5d). A previous report has provided a comprehensive study on colorimetric methods and other methods for ammonia detection.[41] They also estimated the errors with change in pH for indophenol tests. For neutral and alkaline electrolytes, the standard error is <3% for a wide range of concentration of ammonia. However, they found that the ammonia predicted in acidic electrolyte is much lesser than actual concentration of ammonia for concentrations above 0.5 ppm (500 µg L^{-1}). This could probably be a reason why we found that least ammonia in acidic electrolyte. We repeated tests using Nessler's reagent in acidic electrolyte in Figure S16, Supporting Information. Indeed, using Nessler's reagent, we found the concentration of ammonia to be higher compared to indophenol test. However, the trend in activity is similar. Even with Nessler's reagent the activity was found to be highest at –0.1 V versus RHE and decreased at higher potentials.

Additionally, Watt and Crisp analysis were also done to test hydrazine may be a byproduct of nitrogen reduction (Figure S17, Supporting Information). A small amount of hydrazine (around 0.005 ppm) was detected at the optimum potential of nitrogen activation when 0.01 M HCl was used as the electrolyte. This is in accordance with our DFT analysis, which predicts hydrazine formation for certain NiN$_x$ active sites with specified coordination. However, no hydrazine was detected in alkaline or neutral electrolyte.

2.6. DFT Calculation to Elucidate Possible Active Sties and Reaction Pathway

To understand the observed activity of the Ni-N$_x$-C catalyst for the NRR, we have carried out the first-principles DFT calculations to elucidate the thermodynamics of the NRR on various Ni-N$_x$ (x = 3 or 4) sites (Figure S18a, Supporting Information)

embedded in a graphene layer. At first, our DFT results in Figure S18, Supporting Information, reveal that NRR could occur on this Ni-N$_3$ site as follows: Unlike the previously reported ZIF-8-derived carbon (CN$_x$) with nitrogen vacancy, there is no barrier for N$_2$ adsorption on Ni-N$_3$ site. First, N$_2$ molecule adsorbes on the top of the central Ni atom in an end-on configuration (Figure S18b, Supporting Information) with one N atom (denoted as proximal N) chelated with Ni by a bond length of 1.76 Å and another N atom (denoted as distal N) tilted along a Ni–N bond of the Ni-N$_3$ site. **Figure 6**a depicts the charge distribution for this N$_2$ adsorption configuration and shows the electron transfer between the adsorbed N$_2$ molecule and the central Ni atom, which results in a binding energy of 1.31 eV between N$_2$ and Ni-N$_3$ site. Subsequently, the distal N of the adsorbed N$_2$ will undergo two hydrogenation steps to form *NNH and *NNH$_2$ (hydrogenated nitrogen intermediates) (Figure S18c,d, Supporting Information). In the lowest-energy configuration of *NNH$_2$, the N≡N bond length has been stretched to 1.29 Å that is 13% longer than that (1.14 Å) of N$_2$ gas molecule. Although the N≡N bond is weakened, it is not expected to break at this stage. In the following, the proximal N of the adsorbed N$_2$ will undergo two hydrogenation steps to form *NHNH$_2$ and *NH$_2$NH$_2$ (Figure S18e,f, Supporting Information). The N≡N bond in *NH$_2$NH$_2$ is elongated to 1.46 Å that is about 28% longer than that of N$_2$ gas molecule, and thus is significantly weakened. As a result, a subsequent hydrogenation on the dismal N is believed to break the N≡N bond and release one NH$_3$ to dissolve in electrolytes (Figure S18g, Supporting Information). Then, a final hydrogenation step leads to the desorption of final product NH$_3$ and revives the Ni-N$_3$ active site for further NRR as shown in Figure S18h, Supporting Information.

In Figure 6b, we plot our computed free energy evolution for the NRR on the Ni-N$_3$ site following the pathway described above. Our computational results show that under 0 V electrode potential, the first two sequential hydrogenation steps on the distal N and the last hydrogenation step on the proximal N require overcoming some free energy barriers. The free
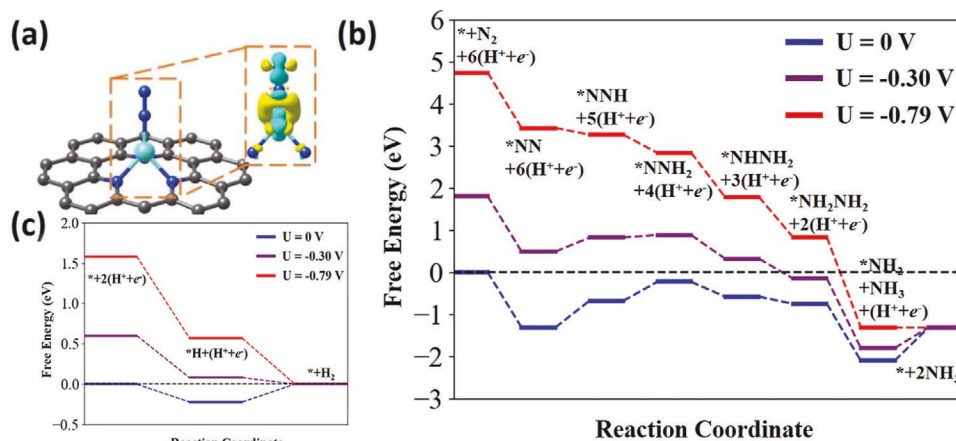
Figure 6. a) Atomistic structure and charge distribution of N$_2$ adsorption on Ni-N$_3$ active site. In this figure, the cyan and yellow clouds show the charge depletion and accumulation; the gray, blue, cyan, and white balls represent the C, N, Ni, and H atoms, respectively. The isosurface was set to be 0.006 eÅ^3. b) Predicted energy evolution of NRR on a Ni-N$_3$ site under applied potential of 0, –0.3, and –0.79 V versus RHE and c) calculated free energy evolution for HER on Ni-N$_3$ active site at 0, –0.3, and –0.79 V versus RHE.

energy barriers for these hydrogenation steps, involving proton and electron charge transfer, could be tuned by externally applied electrode potential. We, therefore, estimated the limiting potential. Limiting potential is the least reversed electrode potential that needs to apply to overcome the largest energy barrier. We found that an electrode potential of −0.79 V is required to proceed the NRR on the Ni-N$_3$ site completely thermodynamically favorable (Figure 6b). The value of this theoretically limiting electrode potential is in good agreement with our experimental value for neutral electrolyte. However, the impact from the electrolyte is a complex topic that includes many factors (e.g., solvation effects, interface structure, effects of electrolyte ions such as K$^+$ and Li$^+$). Such topic will be a good direction for future studies. In our calculations, the effect of electrolytes was not considered. However, we compared the energy barrier for ammonia desorption for Ni-N$_3$ sites and previously reported N4 moiety with N vacancy. At −0.3 V versus RHE, the desorption barrier of last hydrogenation step for Ni-N$_3$ sites is only 0.49 eV compared to 1.44 eV for N4 moiety with N vacancy reported earlier.[5]

Regarding the selectivity of Ni-N$_3$ site for the NRR, we calculated the free energy evolution for the competing HER on the Ni-N$_3$ site as shown in Figure 6c. According to our predicted energy evolution from DFT results, although the adsorption of H$^+$ ion at the active site under 0 V applied potential is also an exothermic reaction with −0.22 eV adsorption energy, the adsorption of N$_2$ at the Ni-N$_3$ site has much lower adsorption energy (−1.31 eV) that can beat the HER. From 0 to −0.79 V applied potential, the adsorption of H$^+$ ion also becomes more and more favored as the free energy change of HER decreases from −0.22 to −1.01 eV Thus, at higher potentials FE decreases. However, we found that the adsorption of N$_2$ on Ni-N$_3$ site was stronger by 0.3 eV than that of H on Ni-N$_3$ site and thus more favorable. Although, hydrogen evolution cannot be completely eliminated, it predicts suppression of HER.

Besides the Ni-N$_3$ site, we computationally examined the free energy evolution of NRR on a more popular Ni-N$_4$ site, in which a Ni-N$_4$ moiety is embedded in a graphene layer, as well as a Ni-N$_{2+2}$ site, in which a Ni-N$_4$ moiety links the edges of two graphene segments. These two types of MN$_4$ sites were found active for oxygen reduction reaction (ORR) and CO$_2$ reduction reaction (CO$_2$RR) in our previous studies on Fe-N-C catalysts.[22,42–47] However, this computational study predicts that the adsorption of N$_2$ on the Ni-N$_4$ site is too weak to initiate the NRR (Figure S19, Supporting Information) and undesired hydrazine (NH$_2$NH$_2$) would be the main product on the Ni-N$_{2+2}$ site by comparing the alternative[48] (Figure S20, Supporting Information) and distal[49] (Figure S21, Supporting Information) pathways in free energy evolution diagram (Figure S22, Supporting Information). Consequently, our computation indicates that the Ni-N$_3$ sites (shown in Figure 6a) are mainly responsible for our experimentally observed good activity and selectivity for the NRR on the atomically dispersed single Ni site (Ni-N-C) catalyst.

3. Conclusions

In summary, we have obtained encouraging NRR activity on atomically dispersed single Ni sites coordinated with three N,

which were prepared from a Ni-doped ZIF-8 precursor through an optimal pyrolysis. The NiN$_3$ site consisting of single Ni coordinated with pyridinic nitrogen and a vacant, favors N$_2$ adsorption, and the NRR activity is much higher than Ni clusters and N-doped carbon obtained under similar pyrolysis condition. The NRR activity was identified universally in alkaline, acidic, and neutral electrolytes, but presents different catalytic activity and selectivity. We verified the coordination of unsaturated Ni using EXAFS and XANES, and explored the structure at the atomic level by using HRTEM and EELS. Moreover, the favorable NRR pathways on different possible configurations of Ni-N$_x$ sites were elucidated using DFT calculations, indicating that a mixed pathway of alternative and enzymatic on Ni-N$_3$-C$_{10}$ configuration is most likely. In addition, on the basis of DFT calculations, the potential determining step during the NRR is the hydrogenation. Thus, this study added insightful knowledge to current "single atom" electrocatalysis, in which such atomically dispersed and nitrogen-coordinated metal sites (MN$_x$) are not only active for the extensively studied ORR and CO$_2$RR, but are also active for the NRR through appropriately designing metal centers and coordination environment.[50]

4. Experimental Section

Catalyst Synthesis: The BMOF of Ni and Zn was synthesized using a previously published procedure where Ni^{2+} replaces some of the Zn^{2+} in the Zn-N$_4$ coordination in ZIF-8 during the crystallization (Figure S1, Supporting Information). Typically, an equal volume of metal nitrate solution in methanol and 2-methylimidazole in methanol was prepared, respectively. Solution of 2-methylimidazole was added to the metal nitrate solution rapidly while stirring by integrating metal into the ligand with a 1:8 ratio and keeping the Ni/Zn molar ratio as 1:1. The mixture was stirred at room temperature and aged for 24 h, followed by centrifugation, washed with ethanol at least three times, and then dried in oven at 60 °C for 6 h. Finally, the obtained BMOF was further subjected to high-temperature treatment (600–1100 °C) under constant N$_2$ flow in a tube furnace with a heating rate of 5 °C min$^{−1}$, designated as Ni-N$_x$-C-T-t, where "T" denotes the temperature of pyrolysis and "t" denotes the time of pyrolysis. For a comparison, control experiments were conducted with Ni clusters on carbon (Ni$_{clusters}$-N-C) and N-doped carbon (N-C) derived from Ni-MOF-74 and ZIF-8 upon pyrolysis under similar conditions, respectively.

Electrochemical Measurements: The catalyst screening was evaluated in a properly sealed single chamber cell with a rotating glassy-carbon-disk electrode (GC-RDE) and a standard three-electrode system with studied catalysts, graphite rod, and Ag/AgCl electrode as the working electrode, counter electrode, and reference electrode, respectively. The reference electrode was calibrated with respect to the RHE by bubbling pure H$_2$ at 1.0 atm into a calibration tube fitted with a Pt wire coated with Pt black. The electrochemical cell was rinsed with 0.1 M H$_2$SO$_4$ solution three times followed by washing with ultrapure water before filling it with 150 mL electrolyte. When preparing the catalyst ink, 10 mg of the catalyst and 30 µL of Nafion were dispersed in 1.0 mL of isopropanol, sonicated for 30 min, and then 20 µL of the ink was dropped onto the GC-RDE with a surface area of 0.245 cm^2. A catalyst loading of 0.8 mg cm^{-2} was used for all of tests.

The electrolyte was saturated with UHP N$_2$ or UHP Ar (control test) for 30 min at the rate of 200 mL min$^{−1}$ before the test to eliminate the dissolved air in electrolyte and then the solution was collected with a syringe to detect any unwanted contamination. Cyclic voltammetry (CV) and LSV were performed at a scan rate of 50 and 5 mV s$^{−1}$, respectively. A sample electrolyte was also collected after CV, LSV, and chronoamperometric tests. Chronoamperometry tests were performed

at different constant potentials.[51,52] The ammonia production rates were calculated by using Equation (1)

$$R_{[NH_3]} = ([NH_3] \times V)/(t \times A) \tag{1}$$

where $[NH_3]$ is the concentration (mol L^{-1}) of ammonia, V is the volume of electrolyte, t is the reaction time, and A is the surface area of the working electrode. Assuming three electrons are consumed to produce one NH_3 molecule, FE was calculated using Equation (2)

$$FE = 3F \times [NH_3] \times V/(17 \times Q) \tag{2}$$

where F is the Faraday constant and Q is the total charge passed through the electrodes during the reaction duration according to the total current density.

Material Characterization: The XRD patterns of the samples were recorded on a Rigaku Ultima IV diffractometer with Cu Kα X-rays operating at 200 mA and 40 kV, using Cu Kα as the radiation source ($\lambda = 0.15418$ nm). A JEOL JEM-2100F field emission electron microscope operating at 200 kV with an EDAX energy dispersive X-ray spectrometer and Nion UltraSTEM U100 operating at 60 kV were used for electron microscopy studies at Oak Ridge National Laboratory (ORNL). The scanning electron microscopy (SEM) images of the samples were taken on a Hitachi SU-70 SEM at a working voltage of 5 kV. Raman spectroscopy was performed using a Renishaw Raman system at 514 nm excitation. Powder samples were deposited on a standard microscope glass slide. XPS was conducted using a Kratos AXIS Ultra DLD XPS system equipped with a hemispherical energy analyzer and a monochromatic Al Kα source operating at 15 keV and 150 W; the pass energy was fixed at 40 eV for the high-resolution scans. Before analysis, the samples were placed in vacuum at 80 °C overnight to remove any adsorbed substances. The specific surface area (S_{BET}) measurements were carried out using N_2 adsorption/desorption at 77 K on a Micromeritics TriStar II instrument. Samples were degassed at 130 °C for 5 h under vacuum prior to nitrogen physisorption measurements. XAS experiments including XANES and EXAFS were carried out at beamline 9-BM, Advanced Photon Source, Argonne National Laboratory. All XAS data were collected in a fluorescence mode and a Vortex ME4 detector was used to collect the Ni K fluorescence signal while the monochromator scanned the incident X-ray photon energy through the Ni K absorption edge. Data reduction, data analysis, and EXAFS fitting were performed with the Athena, Artemis, and IFEFFIT software packages. UV–vis spectra were recorded on a Shimadzu UV-Probe 2600 Series. Accuracies of the obtained results presented here are as follows: ΔN (±10%), ΔR (±1%), $\Delta\sigma^2$ (±10%), and ΔE_0 (±10%).[53] The Ni references used to compare are Ni foil, NiO (Ni^{2+}), and NiOOH (Ni^{3+}).

First-Principles Calculations: The spin-polarized DFT[54–57] calculations, which were performed using the Vienna Ab Initio Simulation package,[58–61] used the Perdew–Burke–Ernzerhof[62] generalized gradient approximation[63] functionals. The van der Waals correction was included using the Tkatchenko–Scheffler method.[64] The plane-wave cutoff energy was set as 400 eV in our calculations. The atomistic structures were relaxed to a tolerance of atomic force below 0.01 eV Å^{-1} during the structural relaxation. A $4 \times 4 \times 1$ Monkhorst–Pack grid[65] was used to sample the Brillouin zone in our DFT calculations. 2D Ni-N$_3$-C catalyst model adopted in our calculations was constructed from a graphene layer and consisted of 28 C atoms, 3 N atoms, and 1 Ni atom with a simulation cell size of 9.84 × 8.52 Å. The doped N and Ni atoms occupied graphitic carbon sites of the graphene layer and formed the Ni-N$_3$ active site with a central Ni atom and three adjacent N atoms. A vacuum layer with a thickness of 18 Å was added in the normal direction to the graphene layer to minimize the interaction between the two periodic images.

At the standard state of the RHE, the free energy of a single pair of electron and proton can be indirectly calculated by the free energy of $\frac{1}{2}$ H$_2$ molecule in gas phase as $G_{H^+} + G_{e^-} = \frac{1}{2} G_{H_2}$.[66] The free energy of each reaction species was calculated with reference to RHE as

$$\Delta G = \Delta E_{ads} + \Delta E_{ZPE} - eU \tag{3}$$

where ΔE_{ads} is the adsorption energy of the reaction species on the NiN$_3$ site, ΔE_{ZPE} is the zero-point energy change computed from the vibrational model, and eU accounts for the energy shift owing to applied electrode potential.

Supporting Information

Supporting Information is available from the Wiley Online Library or from the author.

Acknowledgements

Conflict of Interest

The authors declare no conflict of interest.

Keywords

[1] K. Ithisuphalap, H. Zhang, L. Guo, Q. Yang, H. Yang, G. Wu, *Small Methods* **2019**, *3*, 1800352.

[2] H. Xu, K. Ithisuphalap, Y. Li, S. Mukherjee, J. Lattimer, G. Soloveichik, G. Wu, *Nano Energy* **2020**, *69*, 104469.

[3] G. Soloveichik, *Nat. Catal.* **2019**, *2*, 377.

[4] B. H. R. Suryanto, H.-L. Du, D. Wang, J. Chen, A. N. Simonov, D. R. MacFarlane, *Nat. Catal.* **2019**, *2*, 290.

[5] S. Mukherjee, D. A. Cullen, S. Karakalos, K. Liu, H. Zhang, S. Zhao, H. Xu, K. L. More, G. Wang, G. Wu, *Nano Energy* **2018**, *48*, 217.

[6] X. Yang, K. Li, D. Cheng, W.-L. Pang, J. Lv, X. Chen, H.-Y. Zang, X.-L. Wu, H.-Q. Tan, Y.-H. Wang, Y.-G. Li, *J. Mater. Chem. A* **2018**, *6*, 7762.

[7] Y. Liu, Y. Su, X. Quan, X. Fan, S. Chen, H. Yu, H. Zhao, Y. Zhang, J. Zhao, *ACS Catal.* **2018**, *8*, 1186.

**ADVANCED
SCIENCE NEWS**

www.advancedsciencenews.com

**small
methods**

www.small-methods.com

[8] H. Wang, L. Wang, Q. Wang, S. Ye, W. Sun, Y. Shao, Z. Jiang, Q. Qiao, Y. Zhu, P. Song, D. Li, L. He, X. Zhang, J. Yuan, T. Wu, G. A. Ozin, *Angew. Chem., Int. Ed.* **2018**, *57*, 12360.

[9] Y. Song, D. Johnson, R. Peng, D. K. Hensley, P. V. Bonnesen, L. Liang, J. Huang, F. Yang, F. Zhang, R. Qiao, A. P. Baddorf, T. J. Tschaplinski, N. L. Engle, M. C. Hatzell, Z. Wu, D. A. Cullen, H. M. Meyer, B. G. Sumpter, A. J. Rondinone, *Sci. Adv.* **2018**, *4*, e1700336.

[10] W. Li, J. Huang, L. Feng, L. Cao, Y. Liu, L. Pan, *J. Power Sources* **2018**, *398*, 91.

[11] X. Chen, X. Zhao, Z. Kong, W.-J. Ong, N. Li, *J. Mater. Chem. A* **2018**, *6*, 21941.

[12] L. Han, X. Liu, J. Chen, R. Lin, H. Liu, F. Lu, S. Bak, Z. Liang, S. Zhao, E. Stavitski, J. Luo, R. R. Adzic, H. L. Xin, *Angew. Chem., Int. Ed.* **2019**, *58*, 2321.

[13] X.-F. Li, Q.-K. Li, J. Cheng, L. Liu, Q. Yan, Y. Wu, X.-H. Zhang, Z.-Y. Wang, Q. Qiu, Y. Luo, *J. Am. Chem. Soc.* **2016**, *138*, 8706.

[14] Z. Geng, Y. Liu, X. Kong, P. Li, K. Li, Z. Liu, J. Du, M. Shu, R. Si, J. Zeng, *Adv. Mater.* **2018**, *30*, 1803498.

[15] Q. Qin, T. Heil, M. Antonietti, M. Oschatz, *Small Methods* **2018**, *2*, 1800202.

[16] C. Choi, S. Back, N.-Y. Kim, J. Lim, Y.-H. Kim, Y. Jung, *ACS Catal.* **2018**, *8*, 7517.

[17] A. R. Singh, J. H. Montoya, B. A. Rohr, C. Tsai, A. Vojvodic, J. K. Nørskov, *ACS Catal.* **2018**, *8*, 4017.

[18] Y. He, Q. Tan, L. Lu, J. Sokolowski, G. Wu, *Electrochem. Energy Rev.* **2019**, *2*, 231.

[19] M. Chen, Y. He, J. S. Spendelow, G. Wu, *ACS Energy Lett.* **2019**, *4*, 1619.

[20] B.-W. Zhang, Y.-X. Wang, S.-L. Chou, H.-K. Liu, S.-X. Dou, *Small Methods* **2019**, *3*, 1800497.

[21] J. Li, H. Zhang, W. Samarakoon, W. Shan, D. A. Cullen, S. Karakalos, M. Chen, D. Gu, K. L. More, G. Wang, Z. Feng, Z. Wang, G. Wu, *Angew. Chem. Int. Ed.* **2019**, *58*, 18971.

[22] H. Zhang, S. Hwang, M. Wang, Z. Feng, S. Karakalos, L. Luo, Z. Qiao, X. Xie, C. Wang, D. Su, Y. Shao, G. Wu, *J. Am. Chem. Soc.* **2017**, *139*, 14143.

[23] M. Wang, L. Árnadóttir, Z. J. Xu, Z. Feng, *Nano-Micro Lett.* **2019**, *11*, 47.

[24] H. B. Yang, S.-F. Hung, S. Liu, K. Yuan, S. Miao, L. Zhang, X. Huang, H.-Y. Wang, W. Cai, R. Chen, J. Gao, X. Yang, W. Chen, Y. Huang, H. M. Chen, C. M. Li, T. Zhang, B. Liu, *Nat. Energy* **2018**, *3*, 140.

[25] K. C. Ryan, O. E. Johnson, D. E. Cabelli, T. C. Brunold, M. J. Maroney, *J. Biol. Inorg. Chem.* **2010**, *15*, 795.

[26] L. Zhang, Y. Jia, G. Gao, X. Yan, N. Chen, J. Chen, M. T. Soo, B. Wood, D. Yang, A. Du, X. Yao, *Chem* **2018**, *4*, 285.

[27] T. Zheng, K. Jiang, N. Ta, Y. Hu, J. Zeng, J. Liu, H. Wang, *Joule* **2019**, *3*, 265.

[28] C. Zhao, X. Dai, T. Yao, W. Chen, X. Wang, J. Wang, J. Yang, S. Wei, Y. Wu, Y. Li, *J. Am. Chem. Soc.* **2017**, *139*, 8078.

[29] G. Wu, N. H. Mack, W. Gao, S. Ma, R. Zhong, J. Han, J. K. Baldwin, P. Zelenay, *ACS Nano* **2012**, *6*, 9764.

[30] G. Wu, P. Zelenay, *Acc. Chem. Res.* **2013**, *46*, 1878.

[31] G. Wu, C. M. Johnston, N. H. Mack, K. Artyushkova, M. Ferrandon, M. Nelson, J. S. Lezama-Pacheco, S. D. Conradson, K. L. More, D. J. Myers, P. Zelenay, *J. Mater. Chem.* **2011**, *21*, 11392.

[32] S. Gupta, S. Zhao, X. X. Wang, S. Hwang, S. Karakalos, D. Su, H. Xu, G. Wu, *ACS Catal.* **2017**, *7*, 8386.

[33] L. M. Malard, M. A. Pimenta, G. Dresselhaus, M. S. Dresselhaus, *Phys. Rep.* **2009**, *473*, 51.

[34] A. C. Ferrari, D. M. Basko, *Nat. Nanotechnol.* **2013**, *8*, 235.

[35] L. Ottaviano, S. Di Nardo, L. Lozzi, M. Passacantando, P. Picozzi, S. Santucci, *Surf. Sci.* **1997**, *373*, 318.

[36] C. Yan, H. Li, Y. Ye, H. Wu, F. Cai, R. Si, J. Xiao, S. Miao, S. Xie, F. Yang, Y. Li, G. Wang, X. Bao, *Energy Environ. Sci.* **2018**, *11*, 1204.

[37] H. Wang, N. Yang, W. Li, W. Ding, K. Chen, J. Li, L. Li, J. Wang, J. Jiang, F. Jia, Z. Wei, *ACS Energy Lett.* **2018**, *3*, 1345.

[38] R. Gilliam, J. Graydon, D. Kirk, S. Thorpe, *Int. J. Hydrogen Energy* **2007**, *32*, 359.

[39] A. N. Campbell, E. M. Kartzmark, B. G. Oliver, *Can. J. Chem.* **1966**, *44*, 925.

[40] B. B. Owen, F. H. Sweeton, *J. Am. Chem. Soc.* **1941**, *63*, 2811.

[41] Y. Zhao, R. Shi, X. Bian, C. Zhou, Y. Zhao, S. Zhang, F. Wu, G. I. N. Waterhouse, L.-Z. Wu, C.-H. Tung, T. Zhang, *Adv. Sci.* **2019**, *6*, 1802109.

[42] F. Pan, H. Zhang, K. Liu, D. Cullen, K. More, M. Wang, Z. Feng, G. Wang, G. Wu, Y. Li, *ACS Catal.* **2018**, *8*, 3116.

[43] H. Zhang, H. T. Chung, D. A. Cullen, S. Wagner, U. I. Kramm, K. L. More, P. Zelenay, G. Wu, *Energy Environ. Sci.* **2019**, *12*, 2548.

[44] Y. He, S. Hwang, D. A. Cullen, M. A. Uddin, L. Langhorst, B. Li, S. Karakalos, A. J. Kropf, E. C. Wegener, J. Sokolowski, M. Chen, D. Myers, D. Su, K. L. More, G. Wang, S. Litster, G. Wu, *Energy Environ. Sci.* **2019**, *12*, 250.

[45] J. Li, M. Chen, D. A. Cullen, S. Hwang, M. Wang, B. Li, K. Liu, S. Karakalos, M. Lucero, H. Zhang, C. Lei, H. Xu, G. E. Sterbinsky, Z. Feng, D. Su, K. L. More, G. Wang, Z. Wang, G. Wu, *Nat. Catal.* **2018**, *1*, 935.

[46] X. X. Wang, V. Prabhakaran, Y. He, Y. Shao, G. Wu, *Adv. Mater.* **2019**, *31*, 1805126.

[47] X. X. Wang, D. A. Cullen, Y.-T. Pan, S. Hwang, M. Wang, Z. Feng, J. Wang, M. H. Engelhard, H. Zhang, Y. He, Y. Shao, D. Su, K. L. More, J. S. Spendelow, G. Wu, *Adv. Mater.* **2018**, *30*, 1706758.

[48] B. Hinnemann, J. K. Nørskov, *J. Am. Chem. Soc.* **2004**, *126*, 3920.

[49] R. R. Schrock, *Philos. Trans. R. Soc., A* **2005**, *363*, 959.

[50] Y. Zhu, J. Sokolowski, X. Song, Y. He, Y. Mei, G. Wu, *Adv. Energy Mater.* **1902844**.

[51] H. Verdouw, C. Van Echteld, E. Dekkers, *Water Res.* **1978**, *12*, 399.

[52] W. Bolleter, C. Bushman, P. W. Tidwell, *Anal. Chem.* **1961**, *33*, 592.

[53] Z. Feng, Q. Ma, J. Lu, H. Feng, J. W. Elam, P. C. Stair, M. J. Bedzyk, *RSC Adv.* **2015**, *5*, 103834.

[54] P. Hohenberg, W. Kohn, *Phys. Rev.* **1964**, *136*, B864.

[55] W. Kohn, L. J. Sham, *Phys. Rev.* **1965**, *140*, A1133.

[56] R. G. Parr, W. Yang, *Density-Functional Theory of Atoms and Molecules*, Vol. 16, Oxford University Press, Oxford **1989**.

[57] R. M. Martin, *Electronic Structure: Basic Theory and Practical Methods*, Cambridge University Press, Oxford **2004**.

[58] G. Kresse, J. Hafner, *Phys. Rev. B* **1994**, *49*, 14251.

[59] G. Kresse, J. Furthmüller, *Phys. Rev. B* **1996**, *54*, 11169.

[60] G. Kresse, J. Furthmüller, *Comput. Mater. Sci.* **1996**, *6*, 15.

[61] G. Kresse, D. Joubert, *Phys. Rev. B* **1999**, *59*, 1758.

[62] J. P. Perdew, K. Burke, M. Ernzerhof, *Phys. Rev. Lett.* **1996**, *77*, 3865.

[63] J. P. Perdew, J. Chevary, S. Vosko, K. A. Jackson, M. R. Pederson, D. Singh, C. Fiolhais, *Phys. Rev. B* **1992**, *46*, 6671.

[64] A. Tkatchenko, M. Scheffler, *Phys. Rev. Lett.* **2009**, *102*, 073005.

[65] H. J. Monkhorst, J. D. Pack, *Phys. Rev. B* **1976**, *13*, 5188.

[66] J. K. Nørskov, J. Rossmeisl, A. Logadottir, L. Lindqvist, J. R. Kitchin, T. Bligaard, H. Jonsson, *J. Phys. Chem. B* **2004**, *108*, 17886.